



HAL
open science

Nanostructured “ Fe₂O₃/nickel-based co-catalyst” electrode materials for the photoelectrochemical oxidation of urea in wastewaters

Assia Karrab, Rémi Bensimon, D. Muller-Bouvet, Stéphane Bastide, Christine Cachet-vivier, Salah Ammar

► **To cite this version:**

Assia Karrab, Rémi Bensimon, D. Muller-Bouvet, Stéphane Bastide, Christine Cachet-vivier, et al.. Nanostructured “ Fe₂O₃/nickel-based co-catalyst” electrode materials for the photoelectrochemical oxidation of urea in wastewaters. Applied physics. A, Materials science & processing, 2022, 128 (12), pp.1067. 10.1007/s00339-022-06221-5 . hal-04298276

HAL Id: hal-04298276

<https://hal.science/hal-04298276>

Submitted on 21 Nov 2023

HAL is a multi-disciplinary open access archive for the deposit and dissemination of scientific research documents, whether they are published or not. The documents may come from teaching and research institutions in France or abroad, or from public or private research centers.

L'archive ouverte pluridisciplinaire **HAL**, est destinée au dépôt et à la diffusion de documents scientifiques de niveau recherche, publiés ou non, émanant des établissements d'enseignement et de recherche français ou étrangers, des laboratoires publics ou privés.

Nanostructured «Fe₂O₃/nickel-based co-catalyst» electrode materials for the photoelectrochemical oxidation of urea in wastewaters

Assia Karrab¹, Remi Bensimon², Diane Muller-Bouvet², Stéphane Bastide², Christine Cachet-Vivier², Salah Ammar¹

¹ Unite de Recherche Electrochimie, Materiaux Et Environnement UREME (UR17ES45), Faculte Des Sciences de Gabes, Universite de Gabes, Cite Erriadh, 6072 Gabes, Tunisia

² Universite Paris Est, ICMPE (UMR 7182), CNRS, UPEC, F- 94320, Thiais, France

Abstract

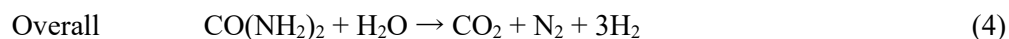
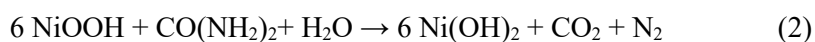
The electrochemical and photoelectrochemical (PEC) properties of undoped, Ni-doped hematite nanoparticles and the film Ni-Fe₂O₃/Ni, a photoactive semiconductor, were investigated utilizing a methodology that combined the co-precipitation approach, spin-coating method and the sputtering-assisted synthesis of Fe₂O₃, Ni-Fe₂O₃, and Ni-Fe₂O₃/Ni, respectively. The excellent oxygen evolution reaction (OER) response was observed for 15% Ni-Fe₂O₃. The super capacitive properties of Ni-Fe₂O₃ at a scan rate of 10 mVs⁻¹ show a maximum super capacitance of 914.76 F/g. The electrochemical oxidation of water achieved by Ni-Fe₂O₃@GCE modified electrode exhibited the current density of 1.5 mA/cm² at 1.5 V vs. the reversible hydrogen electrode (RHE) for 15% of Ni and reveals enhanced specific capacitance of 914.76 F/g. In another part, this work reported the photoelectrochemical (PEC) properties of undoped and 15% Ni-Fe₂O₃ photoanodes. A photocurrent 1.8 and 0.35 μA/cm² at 1.5 V vs. RHE was obtained for undoped and 15% Ni-doped hematite, respectively. It is worth to note that the oxidation current density of 15% Ni-Fe₂O₃/Ni reached 300 μA/cm² at 1.6 V, which is greater than three times of the highest current density than in water (100 μA/cm²).

Keywords Hematite: Urea, Nickel, Water splitting, Photoelectrochemical urea oxidation

1 Introduction

So far, in a photoelectrochemical (PEC) device, many important materials have been explored in the form of photoanodes such as Fe₂O₃ [1], WO₃ [2], BiVO₄ [3], TiO₂ [4], and ZnO [5]. As a promising candidate material for the fractionation of PEC water, Fe₂O₃, a promising semiconductor metal oxide, has received a lot of attention due to its admirable characteristics such as non-toxicity, excellent stability, economical,

chemically synthesized, stable and profitable, low cost, its high corrosion resistance and its moderate difference (~ 2 eV) [6, 7] allowing capturing $\sim 40\%$ of sunlight, environmentally friendly, and widely used in photocatalysis [8], water treatment [9], water splitting [10], magnetic devices [11], Li-ion batteries [12, 13], imaging [14], biosensing [15, 16], drug delivery [17], and fuel cells [18]. Wastewater rich in urea poses a serious environmental and health problem due to the natural conversion of urea to harmful ammonia through the hydrolysis process [19, 20]. Urea can be spread in the environment from the wastewater of production plants, by leaching from livestock farms and by the effluents of plants that use urea as a raw material. However, the daily production of urea of an average adult is approximately 33 g [21] as well as the principal constituent of human or animal waste on earth is urine, containing approximately 2 to 2.5% in weight of urea [20]. So handling wastewater is urgent and electrooxidation of urea is considered an effective approach. Electro-oxidation products of urea in the form of gases such as nitrogen and carbon dioxide are harmless to the environment. As a potential source of hydrogen and fuel, urea has a high energy density (16.9 MJ/L), a high solubility (1079 g/L, 20 °C) [22], and a content of relatively high hydrogen (10.1% by weight) [23]. Electrochemical oxidation of urea to hydrogen in alkaline media has significant advantages over standard hydrogen production methods [24]. So far, the noble metals that have been tested; however, their application was limited due to their high cost, numerous studies have shown that nickel, as a non-noble metal, is the first metal electrocatalyst used for the oxidation of urea. Ni-based catalysts such as Ni, NiO, Ni(OH)₂, and Ni-based alloys (Ni / Co, Ni / Mo, Ni / Mn, etc.) are currently reported to be effective catalyst materials for electro-oxidation of urea in alkaline solution [25]. Botte and co-workers have proposed the mechanism for urea oxidation on nickel-based electrode, which follows an indirect, electrochemical – chemical mechanism. The mechanism of urea electro-oxidation with nickel-based catalyst in alkaline media can be expressed as follows [26].



In the current work, we developed new photoanode materials based on hematite for the electrochemical and the photoelectrochemical conversion of urea that are selective, stable, low cost, and high efficiency, Ni-Fe₂O₃ and Ni-Fe₂O₃ /Ni, a photoactive semiconductor, prepared using a process involving a combination of the co-precipitation, spin coating, and sputtering deposition. The purpose of the present work is to gain more insight into the characterization of the electrocatalytic oxidation of urea on Ni-Fe₂O₃ nanoparticles-modified glassy carbon electrode (GCE) in alkaline medium. Particular attention should be paid to the

photoelectrolysis of alkaline urea solutions following the shaping of nanoparticles in film form by the spin-coating method as well as the invention of a sputtering process to produce an ultrathin layer of Ni on the nickel-doped hematite photoanode.

2 Experimental

2.1 Materials

Iron (III) chloride hexahydrate ($\text{FeCl}_3 \cdot 6\text{H}_2\text{O}$, 97%), aqueous ammonia solution (99%) at 28%, nickel (II) chloride hexahydrate ($\text{NiCl}_2 \cdot 6\text{H}_2\text{O}$, 98%), High Surface Area Graphite 500 from TIMCAL (hereafter designated as CG), PTFE, and ethanol were purchased from Sigma-Aldrich. All the solutions were prepared with ultrapure water.

2.2 Synthesis of pure, Ni-doped $\alpha\text{-Fe}_2\text{O}_3$ nanoparticles

The co-precipitation method was used to make nanoparticles of undoped iron oxide (Fe_2O_3) and Ni-doped Fe_2O_3 (1, 5, 7, 9, 10, 15, and 20% molar). For the first step, 0.15 M $\text{FeCl}_3 \cdot 6\text{H}_2\text{O}$ was dissolved in 100 mL ultrapure water for 30 min at 80 °C. After that, different amounts of $\text{NiCl}_2 \cdot 6\text{H}_2\text{O}$ were added to the solution. Then until the solution reached a pH of 11, an aqueous ammonia solution was added and the solution was held for 3 h to entirely get the hydroxide phase. The resulting precipitations were collected and centrifuged at 6000 rpm and washed with distilled water and ethanol for several times, followed by a drying step at 80 °C for 12 h and an annealing process at 800 °C for 4 h.

2.3 Preparation of $\alpha\text{-Fe}_2\text{O}_3$, Ni- Fe_2O_3 nanoparticles-modified glassy carbon electrode (GCE)

The glassy carbon electrode (GCE) with a surface area of 0.071 cm², was polished with 0.3 and 0.5 μm alumina slurry to a mirror surface [27] with the help of a polishing microfiber cloth, respectively, and then sonicated in ethanol and finally in water before drying [28]. The dispersion of 20 mg of active electrocatalysts in 40 mg of absolute ethanol with 2% carbon (High Surface Area Graphite 500 M²g⁻¹) and 4% PTFE was then tested. To obtain a homogenous mixture, the active ingredients were thoroughly disseminated in 2.4 g of water using ultrasonication for 1 h. It was then drop casted onto a cleaned GCE with a homogeneous mixture of 10 μL loaded on the surface. To examine additional electrochemical characterization, the manufactured modified electrode was let to dry for 15 min at 50 °C (Scheme 1A).

2.4 Preparation of the Fe_2O_3 , Ni- Fe_2O_3 , and Ni- $\text{Fe}_2\text{O}_3/\text{Ni}$ films

To test the PEC performance of the synthesized Ni-doped Fe_2O_3 , a fluorine-doped tin oxide (FTO) glass plate was first ultrasonicated in ethanol and water for 30 min. Then a suspension containing 3.2 mg of

sample (Fe_2O_3 or $\text{Ni-Fe}_2\text{O}_3$ prepared by co-precipitation method (Sect. 2.2)), 0.5 mL of ethanol, and 0.5 mL of deionized water was ultrasonicated for 45 min to obtain a suspension that was applied to the FTO plate using a 150 mL pipette in the active area of 1x2 cm by spin coating (300 rpm for 50 s) and then calcined at 800 °C to obtain a photoanode ready to take PEC measurements (Scheme 1B). Direct current (DC) sputtering technique was used to deposit a Ni layer (1 nm) on the surface of FTO/15% $\text{Ni-Fe}_2\text{O}_3$. Sputtering took place in argon environment. The pressure and current were kept at 0.04 KPas and 40 mA, respectively (Scheme 1C) [29].

2.5 Characterization techniques

The crystal structure and purity of the synthesized pristine and Ni-doped $\alpha\text{-Fe}_2\text{O}_3$ were confirmed by powder XRD analysis using a D8 ADVANCE Bruker diffractometer ($\text{Cu K}\alpha$ radiation). The morphology was observed by SEM with a Merlin FEG microscope from Zeiss and the presence of Ni in $\text{Ni-Fe}_2\text{O}_3$ was confirmed by EDX analysis. Fourier transform infrared (FTIR) spectra of samples were explored by a NICOLET IR200 FTIR spectrometer with transmission from 4000 to 400 cm^{-1} , to confirm the functional groups and co-ordination. Diffuse reflectance spectra were recorded in solid state using UV-Vis spectrophotometer U-4100 DEGETAL.

2.6 Electrochemical and photoelectrochemical measurements Electrochemical measurements were performed in a traditional three-electrode cell utilizing an AUTOLAB PGSTAT 100 potentiostat operated by General Purpose Electrochemical System (GPES) software to assess the samples oxygen evolution reaction (OER) activity. The working electrode was a glassy carbon electrode, while the counter and reference electrodes were platinum (Pt) wire and calomel electrode saturated with KCl (SCE), respectively. The electrochemical performance of OER activity was studied using cyclic voltammetry (CV), linear sweep voltammetry (LSV), and chronoamperometry (CA). All tests were carried out with a 1 M NaOH electrolyte in the presence and absence of urea (0.1 M). With a 500 W/m^2 OSRAM spot as a light source, the curves were obtained in both dark and light illumination. The potential was calculated against the reversible hydrogen electrode (RHE) using the following Nernst equation: where ERHE is the potential vs. RHE, E Ag/AgCl is the measured potential against the Ag/AgCl reference electrode, and $E_0 \text{ Ag/AgCl}$ is 0.1976 V at 25 °C.

3 Results and discussion

3.1 Structural analysis The XRD spectra of the bare and Ni-doped rhombohedral hematite structure generated using the co-precipitation approach are shown in Fig. 1. All of the XRD peaks were well linked

to the hematite of JCPDS card number #33-0664 [30]. Diffraction peaks centered at 24.4°, 32.7°, 35.5°, 40.8°, 49.1°, 54.07°, 57.5°, 62.09°, 64.1°, and 69.7° correspond to the crystallographic planes (012), (104), (110), (113), (024), (116), (018), (214), (300), and (1010), respectively. Furthermore, the distinctive peaks identified for Ni-doped hematite nanoparticles at $2\theta = 43.3^\circ$ and 62.5° match to NiO (JCPDS No. 65–2901) (200) and (220) reflections [31]. This proved that Ni ions were doped into hematite nanoparticles. The average crystallite size was determined using the Debye–Scherer formula [9]: $D = 0.9\lambda/(\beta\cos\theta)$, where λ , β , and θ stand for wavelength of X-ray, full-width at half maximum intensity, and Bragg’s angle, respectively. The average crystallite size of the synthesized samples calculated from Debye–Scherer formula is represented in Table 1.

3.2 SEM observations/EDX Scanning electron microscopy was used to examine the morphology and structure of the samples. Microscopic observations of our samples show that crystallites of undoped and Ni-doped hematite indicate the presence of agglomerates composed by a non-uniform distribution of grains with spherical-shaped nanoparticles and nanometric size for the different synthesized compounds (Fig. 2a–h). The EDX spectra of Ni-doped Fe₂O₃ nanostructures are shown in Fig. 2i. The elements present in the produced nanostructures, as well as the purity of the samples, have been confirmed. It confirmed the development of undoped and Ni-doped Fe₂O₃ nanostructures by revealing the presence of Fe, O, and Ni (Table 2).

3.3 Fourier transform infrared (FTIR) spectroscopy The FTIR spectrum of as-prepared iron oxide nanoparticles is shown in Fig. 3 in the range 400–4000 cm^{–1}. This measurement was made to confirm the high purity of the sample. The band at 3500 cm^{–1} is assigned to adsorbed water [32–34]. Other bands are as follows: 515 cm^{–1} for Fe–O stretching mode of hematite and 468 cm^{–1} for lattice mode of FeO₆ [35]. The same results were obtained for Ni-doped α -Fe₂O₃. There are two characteristic bands at 515 and 468 cm^{–1} corresponding to stretching oxygen–metal vibration at tetrahedral (O–Fe–O) and octahedral sites (O–Fe–O and O–Ni–O), respectively. The shifts observed for the above samples may be due to the particle size effect [32].

3.4 Optical analysis The band gap was determined using a UV–Vis spectrophotometer to measure the diffuse reflectance to explore the influence of the percentage of doping on the optical characteristics of α -Fe₂O₃. The reflectance spectra of the hematite photoanodes were measured in the range of 450–800 nm. The diffuse reflectance spectra of α -Fe₂O₃ and Ni-Fe₂O₃ are reported in Fig. 4. The modified Kubelka–Munk function (Eq. 7) was used to produce the corresponding band gaps, as illustrated in Fig. 4b [36].

$$F(R_\infty) \equiv \frac{(1 - R_\infty)^2}{2R_\infty} = \frac{K}{S} \quad (5)$$

$F(R_\infty)$ is the so-called remission or Kubelka–Munk function, where $F(R_\infty) = R_{\text{sample}} = R_{\text{standard}}$. The band gap E_g and absorption coefficient of a direct band gap semiconductor is connected in the parabolic band structure by the well-known equation (6):

$$\alpha h\nu = C_1 (h\nu - E_g)^2 \quad (6)$$

where α is the linear absorption coefficient of the material, $h\nu$ is the photon energy and C_1 is proportionality constant. The K–M absorption coefficient K gets equal to 2 ($K = 2$) when the material scatters perfectly diffusely. In this case, considering the K–M scattering coefficient S as constant with respect to wavelength, and using the remission function in Eq. (6), we obtain the expression:

$$\left[\frac{(1 - R_\infty)^2}{2R_\infty} h\nu \right]^2 = C_2 (h\nu - E_g) \quad (7)$$

Therefore, obtaining $F(R)$ from Eq. (5) and plotting the $[F(R) h\nu]^2$ against $h\nu$, the band gap E_g of a powder sample can be extracted easily. The gap energy of $\alpha\text{-Fe}_2\text{O}_3$ (2.11 eV) is close to the band gap values reported in the literature, which range from 2.0 to 2.2 eV. Optical absorption in the visible range has shown that $\alpha\text{-Fe}_2\text{O}_3$ has immense potential as a photoanode material. The values obtained for the band gap energies of the undoped and Ni-doped Fe_2O_3 nanoparticles are represented in Table 3. Ni-doped $\alpha\text{-Fe}_2\text{O}_3$ powders showed an optical band gap decrease from 2.11 to 1.9 eV when the nickel concentration increased up to 20% Ni. These phenomena suggest that the conduction band edge of Fe_2O_3 is slightly affected by doping of Ni^{2+} . This agrees with the results reported on Ni-doped hematite nanoparticles prepared by other techniques [37]. This can be attributed to the magnetic properties and improvement of the electrical surface conductivity of Ni- Fe_2O_3 [38].

3.5 Electrochemical measurement

In 1 M NaOH alkaline solution in the absence/presence of urea (0.1 M), the full electrochemical investigations were carried out using SCE as a reference electrode, platinum wire as a counter electrode, and the active material-coated GCE as a working electrode. The following redox reaction [39] made hematite one of the most attractive options for prospective application with the ability to the withstanding pseudocapacitance and normal electric double-layer capacitance:



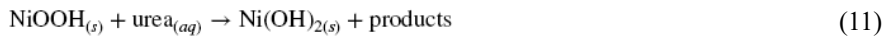
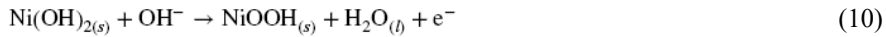
The specific capacitance is the phenomenon which completely supports the efficient electrocatalyst to produce improved oxygen (O₂) evolution (OER) analysis of the respective samples [28]. Hence, the specific capacitance has been calculated from the formula [40],

$$C = \frac{\int_{V_1}^{V_2} I(V) dV}{(V_2 - V_1)Sm} \quad (9)$$

where $I(V) dV$ the area of the CV curve, the mass of the active material (m) layered on the graphite substrate, the scan rate value (S) and the potential window difference ($V_2 - V_1$) have been substituted in the above formula. Table 4 shows the results of the experiment. According to the formula, the sample 15% Ni-Fe₂O₃ has the highest specific capacitance, and the same sample should have the maximum OER activity. The specific capacities for α -Fe₂O₃ in alkaline medium and urea (Fig. 5) are low when compared to those reported in the literature. According to Abdi and al, this can be attributed to the processing temperature of α -Fe₂O₃ (800 °C). Then an inverse relationship between the processing temperature and the specific capacity was confirmed [41].

Furthermore, there was a decrease in ionic conductivity due to the decrease in the hydrated state, as well as a decrease in both the electrolyte's accessibility to the pores and the oxide's reactivity [42]. The percentage of dopant may be responsible for the overall improvement in specific capacity and electrochemical performance of Ni-doped hematite compared to the undoped sample. The doped Fe₂O₃@ GCE electrodes have a higher specific capacitance than the undoped Fe₂O₃@ GCE electrodes due to the electron transport mechanism and electrical conductivity of the doped Fe₂O₃@ GCE electrodes. In reality, the undoped electrode's electron transport kinetics has limited its performance in weaker ones, which removes the electrode's electrochemical processes at the electrode/electrolyte interface [43].

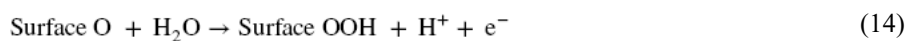
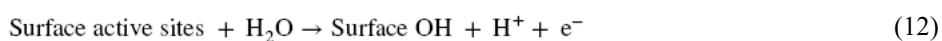
An oxidation peak was observed in the forward scans (Fig. 5a), respectively, for 15% Ni-Fe₂O₃@GCE and 20% Ni-Fe₂O₃@GCE with highest specific capacitance equal to 914.76 F/g for 15% Ni-Fe₂O₃@GCE. In presence of urea (Fig. 5b), a progressively increasing specific capacitance was observed with the increasing percentage of doping such that the highest specific capacitance was observed with a 15% Ni, accompanied with a pairs of redox peaks, which implies the reversibility of the NiOOH/Ni(OH)₂ peak; the regeneration of the Ni(OH)₂ catalyst will lead to the loss of reversibility of the NiOOH/Ni(OH)₂ peak and hence the anodic current density increases drastically [44, 45]:



With increasing nickel oxide content in the manufactured electrocatalyst, higher oxidation current density values were found. The hematite-doped 15 wt% Ni has the maximum oxidation current density. Higher

nickel concentrations (20 wt%) resulted in decreased oxidation current density [45]. This phenomenon can be ascribed to that the excess nickel affects the permeation and oxidation of water [9].

Figure 5c, d shows linear sweep voltammograms of synthesized samples in 1 M NaOH aqueous solution in the absence and presence of urea at a scan rate of 10 mV/s. On the Ni-Fe₂O₃ surface, we may analyze the oxidation of water and urea. Ni-Fe₂O₃ demonstrated its suitability as OER active catalysts for electrochemical water oxidation. Due to the appropriate dopant concentration, the pure phase and quality of the product also enable improved electrical conductivity and increased electron transfer, which can It shows that the sample with the highest specific capacitance has a high OER activity, which could be due to increased electron transfer and the formation of new active centers on the hematite nanostructure due to Ni doping, as demonstrated by Norskov and his co-workers [46] method for analyzing the complete water oxidation process, which occurs via four discrete electron transfer steps as follows:



The excellent electrochemical performance of Ni-Fe₂O₃ demonstrated its suitability as OER active catalysts for electrochemical water oxidation. Due to the appropriate dopant concentration, the pure phase and quality of the product also enable improved electrical conductivity and increased electron transfer, which can explain the enhanced OER activity of the sample synthesized. As well as faster ionic mobility can be explained by the increased active sites expected due to the nanosize combined morphology favoring more electrolyte ion interaction, which improved redox kinetics to some extent [47].

In the literature, a comparison was made with pseudocapacitive nickel-based nanomaterials, where the reversible capacitance of previously described materials was typically in the range of 900–1400 F/g [48]. The capacity of our sample is 914.76 F/g.

When compared to other materials used for electrochemical oxidation of water, such as CuO (doped Co, Ni, and Zn) [40] and WO₄ (doped Co, Cu, Mn, and Zn) [39], the electrochemical oxidation of water obtained by a modified Codoped CuO @ GCE electrode exhibited a current density of 4.41 mA/g at 2.1 V relative to RHE, and the electrochemical OER activity of the 15% Ni-Fe₂O₃ exhibits a current density of 37.6 mA/g (1 M NaOH) (Table 5).

3.6 Photoelectrochemical measurement

To investigate the photoelectrochemical oxidation performance of urea, photoelectrochemical experiments of the α -Fe₂O₃, Ni-Fe₂O₃, and Ni-Fe₂O₃/Ni films were carried out in an aqueous solution of 1.0 M NaOH with or without urea under 500 W/m² illumination light. Spin coating and annealing at 800 °C were used to create the films.

Figure 6 shows the linear scan voltammograms of α -Fe₂O₃ under light and in the dark. In 1 M NaOH with 0.1 M urea, α -Fe₂O₃ has a photocurrent density of 1.8 μ A/cm² at 1.5 V vs. RHE and 1.7 μ A/cm² in 1 M NaOH with 0.1 M urea.

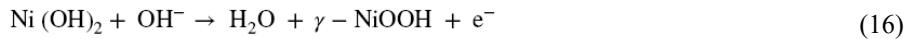
Photocurrent tests were performed to understand the electron transfer in the as-prepared samples (Fig. 6a, b). However, the photocurrent density of the α -Fe₂O₃/FTO electrode reached $\sim 2 \mu$ A cm⁻². The great enhancement of the photocurrent for this electrode compared with the other ones [7, 49, 50], synthesized by a similar method, is due to the good light absorption, efficient electron transfer, and charge separation of the α -Fe₂O₃/FTO nanocomposite. This photoreaction is apparently sensitive to urea in the solution. According to Abdul Hai Alami and these collaborators [51] a concentration greater than 0.1 M causes a barely perceptible effect on the current density in the form of ionic mobility. As it is known that the presence of urea in the solution of NaOH decreases the viscosity of the solution, and it is proven that this has adverse effects on the diffusion coefficient of the solution. The low ion mobility is a direct consequence of the reduced diffusivity of the solution, and this is reflected in the lower photogenerated current of electrode operation.

The stability and reproducibility of the photocurrent signal are seen in Fig. 6c, d. No overshoot was observed at the start or end of the on/off cycle, indicating that the direction of electron scattering was apparently free of grain boundaries, which can create traps that hinder the movement of electrons and slow down the generation of photocurrents [52]. CV voltammograms of 15% Ni-Fe₂O₃ film that was performed in 1 M NaOH in the absence and presence of 0.1 M urea under 500 W/m² light illumination are shown in Fig. 7a, b, respectively. α -Fe₂O₃ film was prepared by spin coating and annealing temperature of 800 °C. 15% Ni-Fe₂O₃ exhibits a photocurrent density of 0.25 μ A/cm² in the absence of urea and 0.4 μ A/cm² in the presence of urea at 1.5 V vs RHE. A small increase was noticed with the presence of urea where the anode current density increased dramatically at potentials greater than 1.43 V relative to RHE, indicating electrocatalytic oxidation of urea on the electrode, an anode peak appears at 1.5 V vs RHE. Interestingly, an anodic peak is noticed in the reverse scan at 1.5 V vs RHE and is in the urea oxidation region that was seen in the prior scan. The appearance of a urea oxidation peak in the reverse scan can be attributed to the regeneration of active sites on the surface of the electrode which further oxidizes the urea molecules, as can the mechanism of regeneration of the urea (Eqs. 10 and 11) [20].

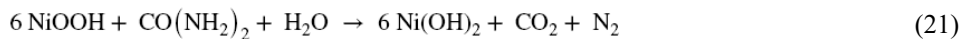
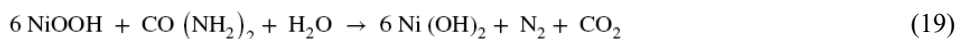
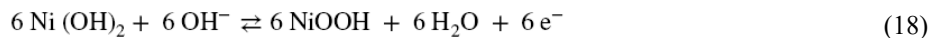
Figure 7c, d depicts the J - V characteristics in both the dark and light illumination for the 15% Ni-doped α -Fe₂O₃ in the presence/absence of urea. Figure 7e shows the photocurrent density for 15% Ni-doped α -Fe₂O₃

electrodes after multiple on/off light cycles. The stability and reproducibility of the photocurrent signal are seen in the figure. No overshoot was observed at the start or end of the on/off cycle, indicating that the direction of electron scattering was apparently free of grain boundaries, which can create traps that hinder the movement of electrons and slow down the generation of photocurrents [52]. As it can be seen, at potential of 1.5 V vs RHE in 1.0 M NaOH electrolyte in the presence and absence of urea, the 15% Ni-Fe₂O₃ photoanode exhibits a weak photocurrent density of 0.4 $\mu\text{A}/\text{cm}^2$ while Fe₂O₃ photoanode yields a photocurrent density of 1.7 $\mu\text{A}/\text{cm}^2$. This drop could be attributed to an overabundance of nickel, which inhibits water penetration and oxidation [53].

The electrode 15% Ni-Fe₂O₃/Ni in 1 M NaOH (Fig. 8a) shows one pair of redox peaks at about 1.5 (oxidation) and 1.3 V (reduction), with a photocurrent response of 28 $\mu\text{A}/\text{cm}^2$ in the oxidation peak and -7.39 $\mu\text{A}/\text{cm}^2$ in the reduction peak, which can be explained by the reversible transformation between Ni(OH)₂ and the species at the redox couple NiOOH [54]. The oxidation of Ni (II) to Ni (III) is shown by the anode peak, while the reduction of Ni (III) to Ni (II) is represented by the cathode peak. According to the literature, the Ni²⁺/ Ni³⁺ transition can take place via two different mechanisms: a solvent mechanism in which nickel oxyhydroxide (γ -NiOOH) is created by OH⁻ diffusion according to Eq. 16, and a proton scattering process in which β -NiOOH is most likely produced (Eq. 17) [55]:

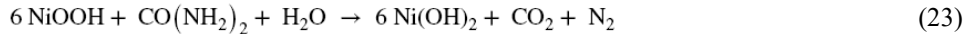


In the presence of urea, a gradual increase in oxidation current occurs as the polarization potential approaches the formation potential of NiOOH, which is around 1.35 V (Fig. 8b). According to the community process, the oxidizing current comes from the oxidative reaction of Ni(OH)₂ to NiOOH, which is aided by urea. The oxidizing current would continue to increase linearly if the electron transfer from Eq. 18 was used to determine the speed rather than mass transfer. The linearly growing oxidizing current in the reducing direction is attributable to the constant oxidative reaction of Ni(OH)₂ to NiOOH, which is not primarily controlled by mass transfer. It is worth noting that the reduction peak of NiOOH to Ni(OH)₂ with urea is lower than without urea, implying that urea consumes some of NiOOH's active sites via an indirect oxidation process (Eq. 19) [56, 57]:



The current density is clearly larger after adding the urea than in the alkaline solution, indicating that the electrodes have good electrocatalytic activity for urea oxidation (Fig. 8c). Ni has a high catalytic activity

for the electrooxidation of urea, as we all know. In an alkaline environment, a thin layer of Ni is applied to the surface of the 15% Ni-Fe₂O₃, which acts as a catalyst for the electrooxidation of urea (Eq. (22) and Eq. (23)) [57]. It is worth noting that at 1.6 V, the oxidation current density of 15% Ni-Fe₂O₃/Ni reached 300 μA/cm², which is more than three times higher than the greatest current density in water (100 μA/cm²).



To further analyze the photoelectrochemical stability, the chronoamperometry graph of 15% Ni-Fe₂O₃/Ni photoanode was recorded at 1.4 V vs RHE for 200 s under on/off illumination with 500 W/m² OSRAM spot as shown in Fig. 9. The photocurrents of the photoanode are stable for this time with a response of photocurrent density equal to 1 μA/cm².

The photocurrent signal exhibits quasi-stability and repeatability throughout on–off cycles of visible light irradiation (Fig. 9), with a rapid current density decline observed during the early stages of chronoamperograms in 1 M NaOH. The current was stable for 200 s after the first decay, which took 50 s. The steady current from 50 to 200 s can be considered substantial confirmation of the produced current's stability, since it follows a steady state behavior for a lengthy time during the experiment. The photocurrents are not stable for this time with a photocurrent density response equal to 1 μA/cm². A photocurrent density of 95% was retained (NaOH + urea), while 13% was retained in the absence of urea, indicating high stability for urea oxidation.

The photocurrent transients were steady, prompt, and reproducible during several on–off cycles of the visible light irradiation as well; no overshoots were observed at the beginning and the end of the flash. The rectangular response shows that the route of electron diffusion was seemingly free of grain boundaries, which can form traps that restrict electron migration and decrease photocurrent generation [58]. The grain boundaries create deep traps to slow down the electron transport and may exist at the particulate electrode. This finding also suggests that the excited electrons are collected efficiently in the external circuit. These results show that Ni-Fe₂O₃ are an excellent sensitizer and hole acceptor, Fe₂O₃ nanoparticles are a bridge, and NiO are an excellent conductive collectors and transporters, all of which play important roles in the photocurrent transient response.

4 Conclusion

This report examined the physical, electrochemical, and PEC properties of Ni-Fe₂O₃/Ni films synthesized with sputtering technique using 15% Ni-Fe₂O₃ synthesized with co-precipitation method. XRD examination revealed the hexagonal crystal structure of the produced nanoparticles, demonstrating that no structural changes occurred after doping with Ni. Ni doping in Fe₂O₃ caused an increase in average grain size. EDX analysis showed the presence of Ni in Ni-Fe₂O₃. Another analysis, such as FTIR and UV–Vis, was carried

out. The electrochemical and photoelectrochemical properties of water and urea electrooxidation were investigated using a variety of methodologies, including CV, LSV, and CA measurements. 15% Ni-Fe₂O₃@GCE electrode has a highest specific capacity equal to 914.76 F/g and a current density equal to 1.126 mAcm⁻² in a solution of 1 M NaOH and 861.57 F/g and a oxidation current density equal to 1.5 mAcm⁻² in the presence of 0.1 M urea. In other circumstances, FTO/ 15%Ni-Fe₂O₃ show a photocurrent density of 0.25 μ A cm⁻² in the absence of urea and 0.4 μ A cm⁻² in the presence of urea at 1.5 V vs. RHE. The FTO /15% Ni-Fe₂O₃/Ni electrode was successfully synthesized by sputtering, the current density of 15% Ni-Fe₂O₃/Ni reached 300 μ A cm⁻² at 1.6 V, which is three times higher than the current density in water (100 μ A cm⁻²). These findings show that the produced Ni-Fe₂O₃/Ni thin film has prospective uses in photocatalysis for water splitting and photoelectrochemical conversion of urea, as well as applications in fuel cells and hydrogen production.

Acknowledgements

The present work was supported by the Research Funds of Electrochemistry, Materials and Environment Research Unit UREME (UR17ES45), Faculty of Sciences Gabes University, Tunisia and Institute of Chemistry and Materials Paris-Est (ICMPE, UMR7182) Thiais, University of Creteil, France.

Declarations

Conflict of interest: The authors declare that they have no conflict of interest.

References

1. A. Annamalai, A. Subramanian, U. Kang, H. Park, S.H. Choi, J.S. Jang, Activation of hematite photoanodes for solar water splitting: effect of FTO deformation. *J. Phys. Chem. C* **119**(7), 3810–3817 (2015)
2. F. Wang, C. Di Valentin, G. Pacchioni, Doping of WO₃ for photocatalytic water splitting: hints from density functional theory. *J. Phys. Chem. C* **116**(16), 8901–8909 (2012)
3. S.S. Dunkle, R.J. Helmich, K.S. Suslick, BiVO₄ as a visible-light photocatalyst prepared by ultrasonic spray pyrolysis. *J. Phys. Chem. C* **113**(28), 11980–11983 (2009)
4. C. Wang, Z. Chen, H. Jin, C. Cao, J. Li, Z. Mi, Enhancing visiblelight photoelectrochemical water splitting through transition-metal doped TiO₂ nanorod arrays. *J. Mater. Chem.* **A2**(42), 17820– 17827 (2014)
5. Y. Hu, X. Yan, Y. Gu, X. Chen, Z. Bai, Z. Kang, Y. Zhang, Largescale patterned ZnO nanorod arrays for efficient photoelectrochemical water splitting. *Appl. Surf. Sci.* **339**, 122–127 (2015)
6. D. Wang, Y. Chen, Y. Zhang, X. Zhang, N. Suzuki, C. Terashima, Boosting photoelectrochemical performance of hematite photoanode with TiO₂ underlayer by extremely rapid high temperature

annealing. *Appl. Surf. Sci.* **422**, 913–920 (2017)

7. V.C. Janu, G. Bahuguna, D. Laishram, K.P. Shejale, N. Kumar, R.K. Sharma, R. Gupta, Surface fluorination of α -Fe₂O₃ using selectfluor for enhancement in photoelectrochemical properties. *Sol. Energy Mater. Sol. Cells* **174**, 240–247 (2018)

8. M. Mishra, D.M. Chun, α -Fe₂O₃ as a photocatalytic material: a review. *Appl. Catal. A* **498**, 126–141 (2015)

9. A. Karrab, L. Lecarme, J.C. Lepretre, A. Nourdine, J. Deseure, S. Ammar, Fe₂O₃ and Fe₂O₃/Ni(OH)₂ photoanodes for highly efficient photoelectrochemical water splitting and urea oxidation. *Appl. Phys. A* **128**(6), 1–11 (2022)

10. T. Tokubuchi, R.I. Arbi, P. Zhenhua, K. Katayama, A. Turak, W.Y. Sohn, Enhanced photoelectrochemical water splitting efficiency of hematite (α -Fe₂O₃)-based photoelectrode by the introduction of maghemite (γ -Fe₂O₃) nanoparticles. *J. Photochem. Photobiol. A Chem.* **410**, 113179 (2021)

11. E.V. Shevchenko, D.V. Talapin, H. Schnablegger, A. Kornowski, O. Festin, P. Svedlindh, H. Weller, Study of nucleation and growth in the organometallic synthesis of magnetic alloy nanocrystals: the role of nucleation rate in size control of CoPt₃ nanocrystals. *J. Am. Chem. Soc.* **125**(30), 9090–9101 (2003)

12. H. Dong, H. Zhang, Y. Xu, C. Zhao, Facile synthesis of α -Fe₂O₃ nanoparticles on porous human hair-derived carbon as improved anode materials for lithium ion batteries. *J. Power Sources* **300**, 104–111 (2015)

13. G. Zhang, Y. Shi, H. Wang, L. Jiang, X. Yu, S. Jing, P. Tsiakaras, A facile route to achieve ultrafine Fe₂O₃ nanorods anchored on graphene oxide for application in lithium-ion battery. *J. Power Sources* **416**, 118–124 (2019)

14. M. Ribeiro, M. Boudoukhani, E. Belmonte-Reche, N. Genicio, S. Sillankorva, J. Gallo, M. Banobre-Lopez, Xanthan-Fe₃O₄ nanoparticle composite hydrogels for non-invasive magnetic resonance imaging and magnetically assisted drug delivery. *ACS Appl. Nano Mater.* **4**(8), 7712–7729 (2021)

15. A. Ahmadivand, B. Gerislioglu, P. Manickam, A. Kaushik, S. Bhansali, M. Nair, N. Pala, Rapid detection of infectious envelope proteins by magnetoplasmonic toroidal metasensors. *ACS Sens.* **2**(9), 1359–1368 (2017)

16. M. Guan, X. Mu, H. Zhang, Y. Zhang, J. Xu, Q. Li, S. Li, Spindlelike Fe₃O₄ nanoparticles for improving sensitivity and repeatability of giant magnetoresistance biosensors. *J. Appl. Phys.* **126**(6), 064505 (2019)

17. A. Tomitaka, H. Arami, A. Ahmadivand, N. Pala, A.J. McGoron, Y. Takemura, M. Nair, Magnetoplasmonic nanostars for image-guided and NIR-triggered drug delivery. *Sci. Rep.* **10**(1), 1–10 (2020)

18. F. Altaf, S. Ahmed, D. Dastan, R. Batool, Z.U. Rehman, Z. Shi, K. Jacob, Novel sepiolite reinforced emerging composite polymer electrolyte membranes for high-performance direct methanol fuel cells. *Mater. Today Chem.* **24**, 100843 (2022)

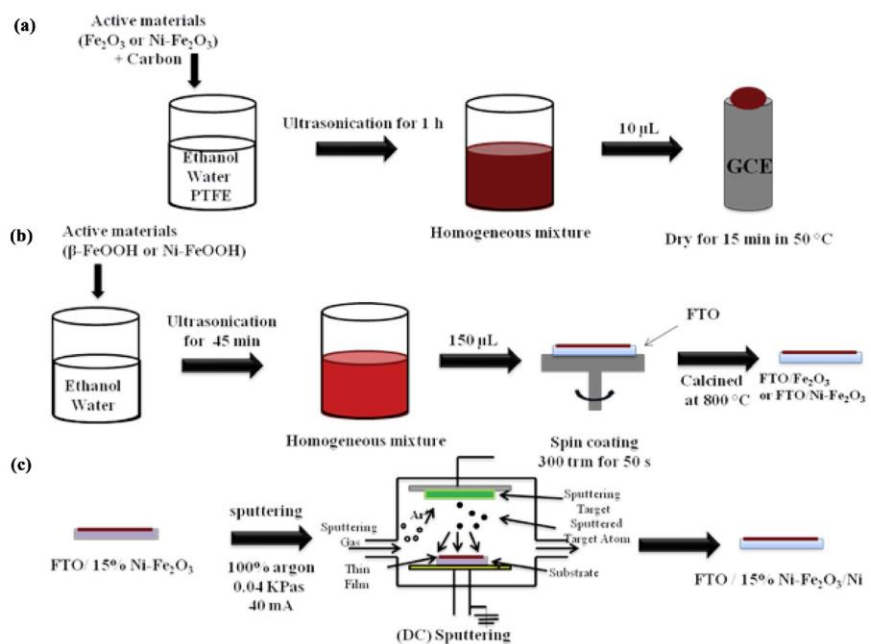
19. M.S. Wu, F.Y. Chen, Y.H. Lai, Y.J. Sie, Electrocatalytic oxidation of urea in alkaline solution using nickel/nickel oxide nanoparticles derived from nickel-organic framework. *Electrochim. Acta* **258**, 167–174 (2017)
20. L. Bian, Q. Du, M. Luo, L. Qu, M. Li, Monodisperse nickel nanoparticles supported on multi-walls carbon nanotubes as an effective catalyst for the electro-oxidation of urea. *Int. J. Hydrog. Energy* **42**(40), 25244–25250 (2017)
21. N. Kakati, J. Maiti, K.S. Lee, B. Viswanathan, Y.S. Yoon, Hollow sodium nickel fluoride nanocubes deposited MWCNT as an efficient electrocatalyst for urea oxidation. *Electrochim. Acta* **240**, 175–185 (2017)
22. A. Ahmadi, A. Nezamzadeh-Ejhieh, A comprehensive study on electrocatalytic current of urea oxidation by modified carbon paste electrode with Ni (II)-clinoptilolite nanoparticles: experimental design by response surface methodology. *J. Electroanal. Chem.* **801**, 328–337 (2017)
23. D.E. Glass, V. Galvan, G.S. Prakash, The effect of annealing temperature on nickel on reduced graphene oxide catalysts on urea electrooxidation. *Electrochim. Acta* **253**, 489–497 (2017)
24. R.L. King, G.G. Botte, Hydrogen production via urea electrolysis using a gel electrolyte. *J. Power Sources* **196**(5), 2773–2778 (2011)
25. G. Das, R.M. Tesfaye, Y. Won, H.H. Yoon, NiO-Fe₂O₃ based graphene aerogel as urea electrooxidation catalyst. *Electrochim. Acta* **237**, 171–176 (2017)
26. D. Wang, W. Yan, S.H. Vijapur, G.G. Botte, Electrochemically reduced graphene oxide–nickel nanocomposites for urea electrolysis. *Electrochim. Acta* **89**, 732–736 (2013)
27. N.S. Arul, D. Mangalaraj, P.N. Kumar, E. Kim, P. Devi, J.I. Han, Synthesis and characterization of α -Fe₂O₃ micro-/nanorodsmodified glassy carbon electrode for electrochemical sensing of nitrobenzene. *Ceram. Int.* **41**(4), 5568–6557 (2015)
28. F.A. Harraz, A.A. Ismail, S.A. Al-Sayari, A. Al-Hajry, M.S. Al- Assiri, Highly sensitive amperometric hydrazine sensor based on novel α -Fe₂O₃/crosslinked polyaniline nanocomposite modified glassy carbon electrode. *Sens. Actuators, B Chem.* **234**, 573–582 (2016)
29. D. Dastan, K. Shan, A. Jafari, F. Gity, X.T. Yin, Z. Shi, L. Ansari, Influence of nitrogen concentration on electrical, mechanical, and structural properties of tantalum nitride thin films prepared via DC magnetron sputtering. *Appl. Phys. A* **128**(5), 1–16 (2022)
30. F. Bouhjar, L. Derbali, B. Mari, B. Bessais, Photo-deposition of cobalt-phosphate group modified hematite for efficient water splitting. *Sol. Energy Mater. Sol. Cells* **195**, 241–249 (2019)
31. Y.W. Phuan, E. Ibrahim, M.N. Chong, T. Zhu, B.K. Lee, J.D. Ocon, E.S. Chan, In situ Ni-doping during cathodic electrodeposition of hematite for excellent photoelectrochemical performance of nanostructured nickel oxide-hematite pn junction photoanode. *Appl. Surf. Sci.* **392**, 144–152 (2017)

32. J. Parhizkar, M.H. Habibi, Synthesis, characterization and photocatalytic properties of iron oxide nanoparticles synthesized by sol-gel autocombustion with ultrasonic irradiation. *Nanochem. Res.* **2**(2), 166–171 (2017)
33. M. Asadzadeh, F. Tajabadi, D. Dastan, P. Sangpour, Z. Shi, N. Taghavinia, Facile deposition of porous fluorine doped tin oxide by Dr. Blade method for capacitive applications. *Ceram. Int.* **47**(4), 5487–5494 (2021)
34. L. Liang, Z. Shi, X. Tan, S. Sun, M. Chen, D. Dastan, L. Cao, Largely improved breakdown strength and discharge efficiency of layer-structured nanocomposites by filling with a small loading fraction of 2D zirconium phosphate nanosheets. *Adv. Mater. Interfaces* **9**(3), 2101646 (2022)
35. A.S. Al-Kady, M. Gaber, M.M. Hussein, E.Z.M. Ebeid, Structural and fluorescence quenching characterization of hematite nanoparticles. *Spectrochim. Acta Part A Mol. Biomol. Spectrosc.* **83**(1), 398–405 (2011)
36. A. Karrab, R. Bensimon, D. Muller, S. Bastide, C. Cachet-Vivier, S. Ammar, Photoelectrochemical and electrochemical urea oxidation with microwave-assisted synthesized Co-Fe₂O₃@NiO core– shell nanocomposites. *Carbon Lett* **32**, 1–17 (2022)
37. R. Suresh, R. Prabu, J.A. Vijayara, K. Giribabu, A. Stephen, V. Narayanan, Facile synthesis of cobalt doped hematite nanospheres: magnetic and their electrochemical sensing properties. *Mater. Chem. Phys.* **134**(2–3), 590–596 (2012)
38. A.E. Morales, E.S. Mora, U. Pal, Use of diffuse reflectance spectroscopy for optical characterization of un-supported nanostructures. *Revista mexicana de fisica* **53**(5), 18–22 (2007)
39. B.J. Rani, G. Ravi, S. Ravichandran, V. Ganesh, F. Ameen, A. Al- Sabri, R. Yuvakkumar, Electrochemically active XWO₄ (X= Co, Cu, Mn, Zn) nanostructure for water splitting applications. *Appl. Nanosci.* **8**(5), 1241–1258 (2018)
40. B.J. Rani, G. Ravi, R. Yuvakkumar, Z.M. Hasan, S. Ravichandran, S.I. Hong, Binder free, robust and scalable CuO@ GCE modified electrodes for efficient electrochemical water oxidation. *Mater. Chem. Phys.* **239**, 122321 (2020)
41. A. Abdi, M. Trari, Investigation on photoelectrochemical and pseudo-capacitance properties of the non-stoichiometric hematite α -Fe₂O₃ elaborated by sol–gel. *Electrochim. Acta* **111**, 869–875 (2013)
42. M.T. Lee, J.K. Chang, Y.T. Hsieh, W.T. Tsai, Annealed Mn–Fe binary oxides for supercapacitor applications. *J. Power Sources* **185**(2), 1550–1556 (2008)
43. Y. Xu, W. Tu, B. Zhang, S. Yin, Y. Huang, M. Kraft, R. Xu, Nickel nanoparticles encapsulated in few-layer nitrogen-doped graphene derived from metal–organic frameworks as efficient bifunctional electrocatalysts for overall water splitting. *Adv. Mater.* **29**(11), 1605957 (2017)

44. X. Zou, Y. Liu, G.D. Li, Y. Wu, D.P. Liu, W. Li, X. Zou, Ultrafast formation of amorphous bimetallic hydroxide films on 3D conductive sulfide nanoarrays for large-current-density oxygen evolution electrocatalysis. *Adv. Mater.* **29**(22), 1700404 (2017)
45. R.A. Hameed, R.H. Tammam, Nickel oxide nanoparticles grown on mesoporous carbon as an efficient electrocatalyst for urea electro-oxidation. *Int. J. Hydrog. Energy* **43**(45), 20591–20606 (2018)
46. C. Ling, L.Q. Zhou, H. Jia, First-principles study of crystalline CoWO₄ as oxygen evolution reaction catalyst. *RSC Adv.* **4**(47), 24692–24697 (2014)
47. B.J. Rani, M.P. Kumar, G. Ravi, S. Ravichandran, R.K. Guduru, R. Yuvakkumar, Electrochemical and photoelectrochemical water oxidation of solvothermally synthesized Zr-doped α -Fe₂O₃ nanostructures. *Appl. Surf. Sci.* **471**, 733–744 (2019)
48. Z. Lu, Z. Chang, J. Liu, X. Sun, Stable ultrahigh specific capacitance of NiO nanorod arrays. *Nano Res.* **4**(7), 658–665 (2011)
49. S. Yin, X. Wang, Z. Mou, Y. Wu, H. Huang, M. Zhu, P. Yang, Synergistic contributions by decreasing overpotential and enhancing charge-transfer in α -Fe₂O₃/Mn₃O₄/graphene catalysts with heterostructures for photocatalytic water oxidation. *Phys. Chem. Chem. Phys.* **16**(23), 11289–11296 (2014)
50. D. Chu, K. Li, A. Liu, J. Huang, C. Zhang, P. Yang, C. Lu, Zn-doped hematite modified by graphene-like WS₂: a p-type semiconductor hybrid photocathode for water splitting to produce hydrogen. *Int. J. Hydrog. Energy* **43**(15), 7307–7316 (2018)
51. A.H. Alami, M.A. Abdelkareem, M. Faraj, K. Aokal, N. Al Safarini, Titanium dioxide-coated nickel foam photoelectrodes for direct urea fuel cell applications. *Energy* **208**, 118253 (2020)
52. M. Sookhakian, Y.M. Amin, S. Baradaran, M.T. Tajabadi, A.M. Golsheikh, W.J. Basirun, A layer-by-layer assembled graphene/ zinc sulfide/polypyrrole thin-film electrode via electrophoretic deposition for solar cells. *Thin Solid Films* **552**, 204–211 (2014)
53. D. Chen, Z. Liu, S. Zhang, Enhanced PEC performance of hematite photoanode coupled with bimetallic oxyhydroxide NiFeOOH through a simple electroless method. *Appl. Catal. B* **265**, 118580 (2020)
54. R.H. Tammam, M.M. Saleh, On the electrocatalytic urea oxidation on nickel oxide nanoparticles modified glassy carbon electrode. *J. Electroanal. Chem.* **794**, 189–196 (2017)
55. H.M. Abd El-Lateef, N.F. Almulhim, A.A. Alaulamie, M.M. Saleh, I.M. Mohamed, Design of ultrafine nickel oxide nanostructured material for enhanced electrocatalytic oxidation of urea: physicochemical and electrochemical analyses. *Colloids Surf., A* **585**, 124092 (2020)
56. F. Guo, K. Ye, M. Du, X. Huang, K. Cheng, G. Wang, D. Cao, Electrochemical impedance analysis of urea electro-oxidation mechanism on nickel catalyst in alkaline medium. *Electrochim. Acta* **210**, 474–482 (2016)

57. G. Wang, Y. Ling, X. Lu, H. Wang, F. Qian, Y. Tong, Y. Li, Solar driven hydrogen releasing from urea and human urine. *Energy Environ. Sci.* **5**(8), 8215–8219 (2012)
58. T. Yoshida, J. Zhang, D. Komatsu, S. Sawatani, H. Minoura, T. Pauporte, H. Yanagi, Electrodeposition of inorganic/organic hybrid thin films. *Adv. Func. Mater.* **19**(1), 17–43 (2009)

FIGURES



Scheme 1. Schematic representation for the synthesis of **A** modified GCE and **B** the films Fe_2O_3 and $\text{Ni-Fe}_2\text{O}_3$ by spin coating and **C** the film of $\text{Ni-Fe}_2\text{O}_3/\text{Ni}$ by sputtering.

Table 1 Calculated crystallite size of the product

Sample	Pos. [$^{\circ}2\theta$]	(h k l)	FWHM [$^{\circ}2\theta$]	Crystallite size (nm)
Undoped	33.21	(1 0 4)	0.229	38
1% Ni-Fe ₂ O ₃	33.03	(1 0 4)	0.19	41
5% Ni-Fe ₂ O ₃	32.96	(1 0 4)	0.24	39
7% Ni-Fe ₂ O ₃	33.19	(1 0 4)	0.17	55
9% Ni-Fe ₂ O ₃	32.92	(1 0 4)	0.20	45
10% Ni-Fe ₂ O ₃	32.99	(1 0 4)	0.17	54
15% Ni-Fe ₂ O ₃	33.18	(1 0 4)	0.18	51
20% Ni-Fe ₂ O ₃	33.18	(1 0 4)	0.18	51

Table 2 The EDX analysis (atomic percent of elements) in the undoped and Ni-doped α -Fe₂O₃ nanoparticles

Sample	O (at %)	Fe (at %)	Ni (at %)
1% Ni-Fe ₂ O ₃	59.33	42.16	0.52
5% Ni-Fe ₂ O ₃	58.15	39.13	2.73
7% Ni-Fe ₂ O ₃	56.13	40.62	3.25
9% Ni-Fe ₂ O ₃	58.44	37.86	3.7
10% Ni-Fe ₂ O ₃	56.79	38.20	5.00
15% Ni-Fe ₂ O ₃	58.49	35.80	5.71
20% Ni-Fe ₂ O ₃	58.77	33.42	7.82

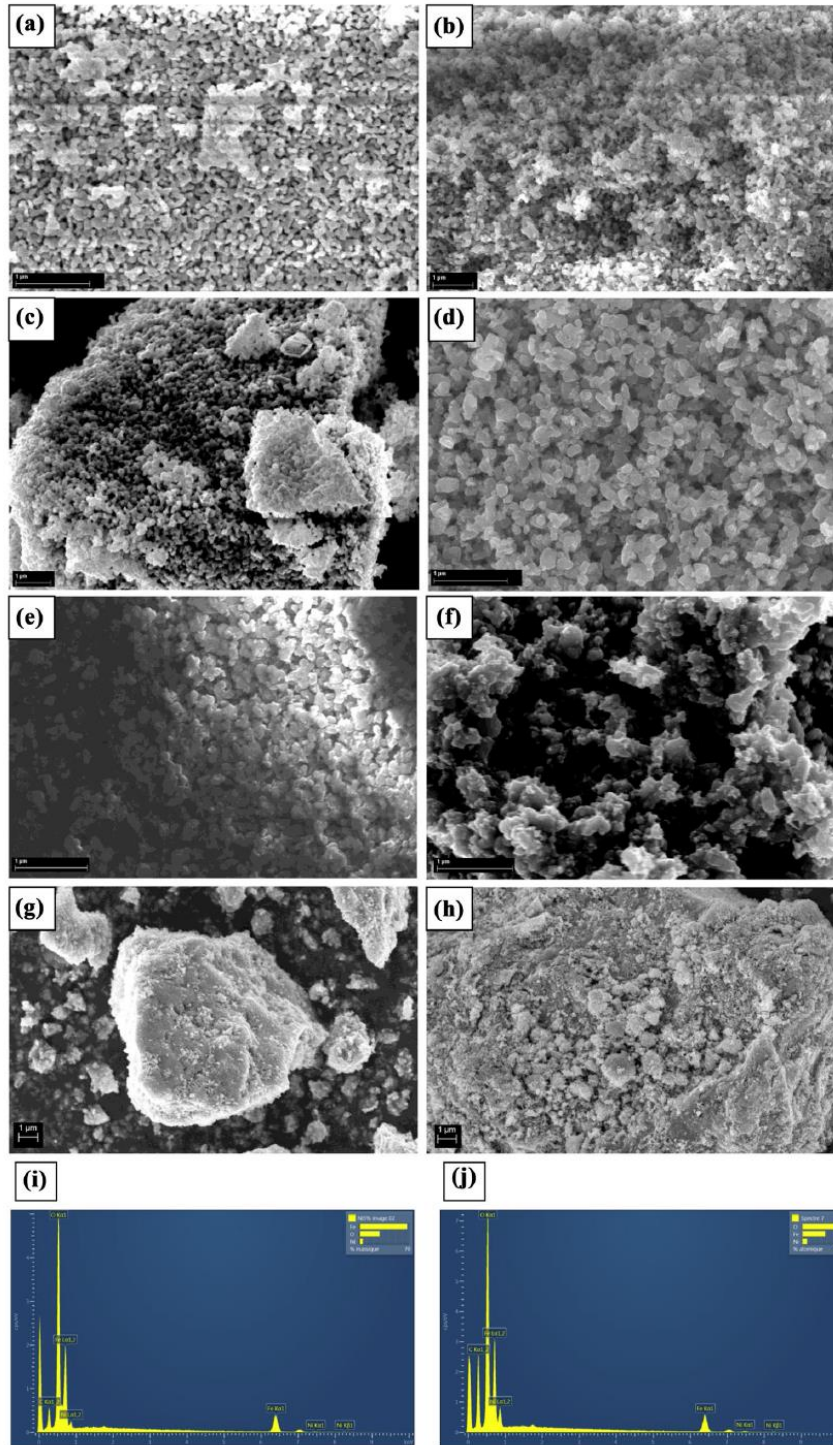


Fig. 2 SEM images of the α -Fe₂O₃ **a** undoped, **b** 1% Ni, **c** 5% Ni, **d** 7% Ni, **e** 9% Ni, **f** 10% Ni, **g** 15% Ni, and **h** 20% Ni; the EDX spectrums for **i** 5% and **j** 10% Ni-doped α -Fe₂O₃.

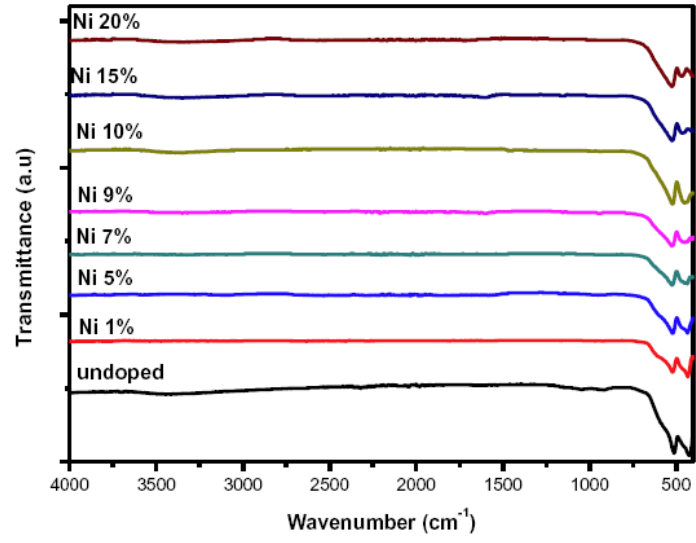


Fig. 3 FTIR spectra of pristine and Ni-doped α -Fe₂O₃.

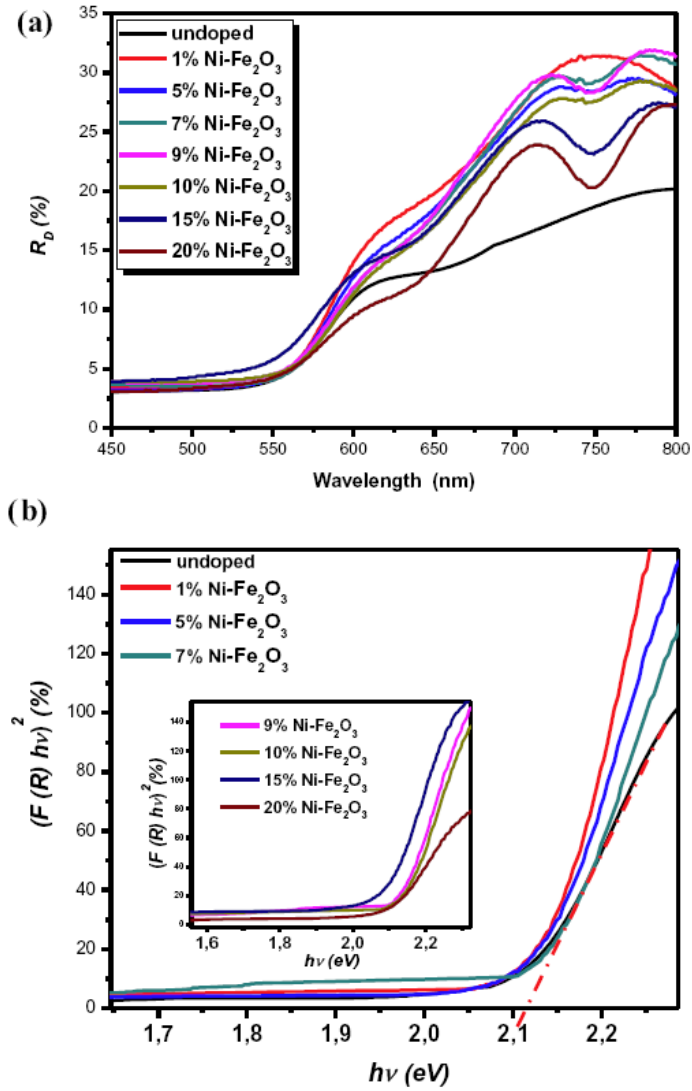


Fig. 4 **a** UV-Vis diffuse reflectance spectra. **b** Band gap profile of undoped and Ni-doped Fe_2O_3 .

Table 3 Band gap of undoped and Ni-doped Fe₂O₃ nanoparticles

sample	Fe ₂ O ₃	1% Ni-Fe ₂ O ₃	5% Ni-Fe ₂ O ₃	7% Ni-Fe ₂ O ₃	9% Ni-Fe ₂ O ₃	10% Ni-Fe ₂ O ₃	15% Ni-Fe ₂ O ₃	20% Ni-Fe ₂ O ₃
Eg (eV)	2.11	2.11	2.10	2.06	1.96	1.95	1.90	1.91

Table 4 Specific capacitance values calculated from CV graph undoped and Ni-doped Fe₂O₃ nanostructures in potential limit of 0.5–1.7 V vs RHE and current density LSV at 1.5 V vs RHE

Sample	Specific capacitance calculated from CV (F/g) at 10 mV/s	Current density LSV at 10 mV/s at 1.5 V vs RHE (mA/g)	Current density LSV at 10 mV/s at 1.5 V vs RHE (mA/cm ²)
NaOH			
α-Fe ₂ O ₃	26.98	1.34 (1.4 V vs. RHE)	0.04 (1.4 V vs. RHE)
1% Ni-Fe ₂ O ₃	94.71	5.1	0.156
5% Ni-Fe ₂ O ₃	218.43	11.9	0.358
7% Ni-Fe ₂ O ₃	112.14	4.6	0.144
9% Ni-Fe ₂ O ₃	32.06	1.51	0.049
10% Ni-Fe ₂ O ₃	37.43	1.11	0.031
15% Ni-Fe ₂ O ₃	914.76	37.6	1.126
20% Ni-Fe ₂ O ₃	687.81	26.8	0.793
NaOH + urea			
α-Fe ₂ O ₃	15.61	0.35 (1.4 V vs. RHE)	0.01 (1.4 V vs. RHE)
1% Ni-Fe ₂ O ₃	12.36	0.7	0.021
5% Ni-Fe ₂ O ₃	31.30	1.7	0.051
7% Ni-Fe ₂ O ₃	44.75	1.02	0.036
9% Ni-Fe ₂ O ₃	47.36	2.7	0.073
10% Ni-Fe ₂ O ₃	145.04	7.2	0.216
15% Ni-Fe ₂ O ₃	861.57	35.9	1.078
20% Ni-Fe ₂ O ₃	273.86	13.6	0.403

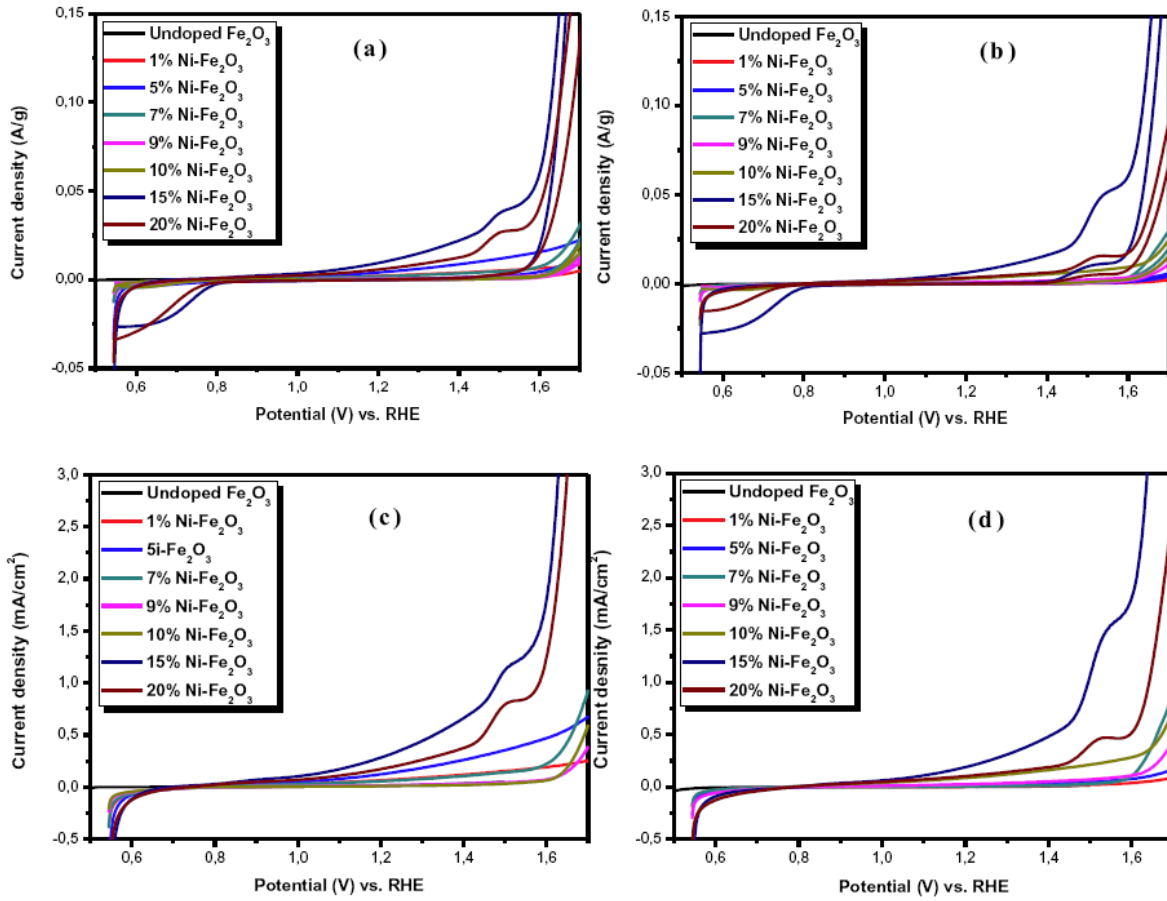


Fig. 5 CV graph a in 1.0 M NaOH, b in NaOH + 0.1 M urea and LSV graph c in 1.0 M NaOH, d in NaOH + 0.1 M urea at scan rate of 10 mVs^{-1} of undoped and Ni-doped Fe_2O_3 .

Table 5. Comparison of electrochemical performance.

Sample	Specific capacitance calculated from CV (F/g) at 10 mV/s	Current density LSV (mA/g)	References
CuO	153	1.25	[40]
Ni-CuO	495	3.92	[40]
Co-CuO	578	4.41	[40]
Zn-CuO	380	2.43	[40]
Co-WO ₄	431	19.87	[39]
Cu-WO ₄	199	12.48	[39]
Mn-WO ₄ (ethanol)	360	55.11	[39]
5% Co-Fe ₂ O ₃	352	21.67	[36]
5% Co-Fe ₂ O ₃ (urea)	44	2.63	[36]
15% Ni-Fe ₂ O ₃	914	37.6	Present work
15% Ni-Fe ₂ O ₃ (urea)	861	35.9	Present work

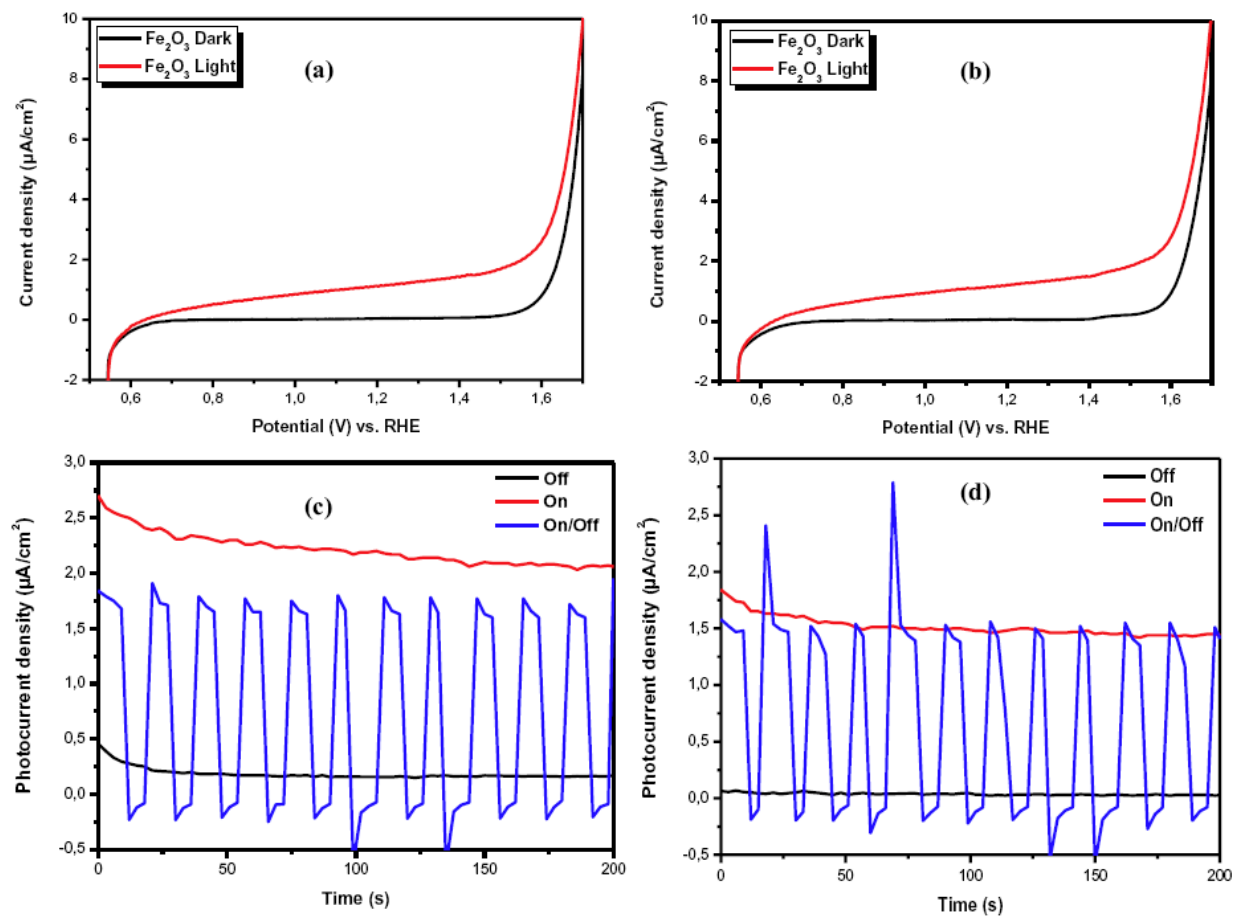


Fig. 6 LSV graph in **a** NaOH (1 M), **b** NaOH + urea (0.1 M) in dark and with illumination at a scan rate of 10 mVs⁻¹ and photocurrent intensity in **c** NaOH (1 M), **d** NaOH + urea (0.1 M) under on/off successive illumination cycles under a bias potential of 1.4 V (vs. RHE) of Fe₂O₃ photoanode.

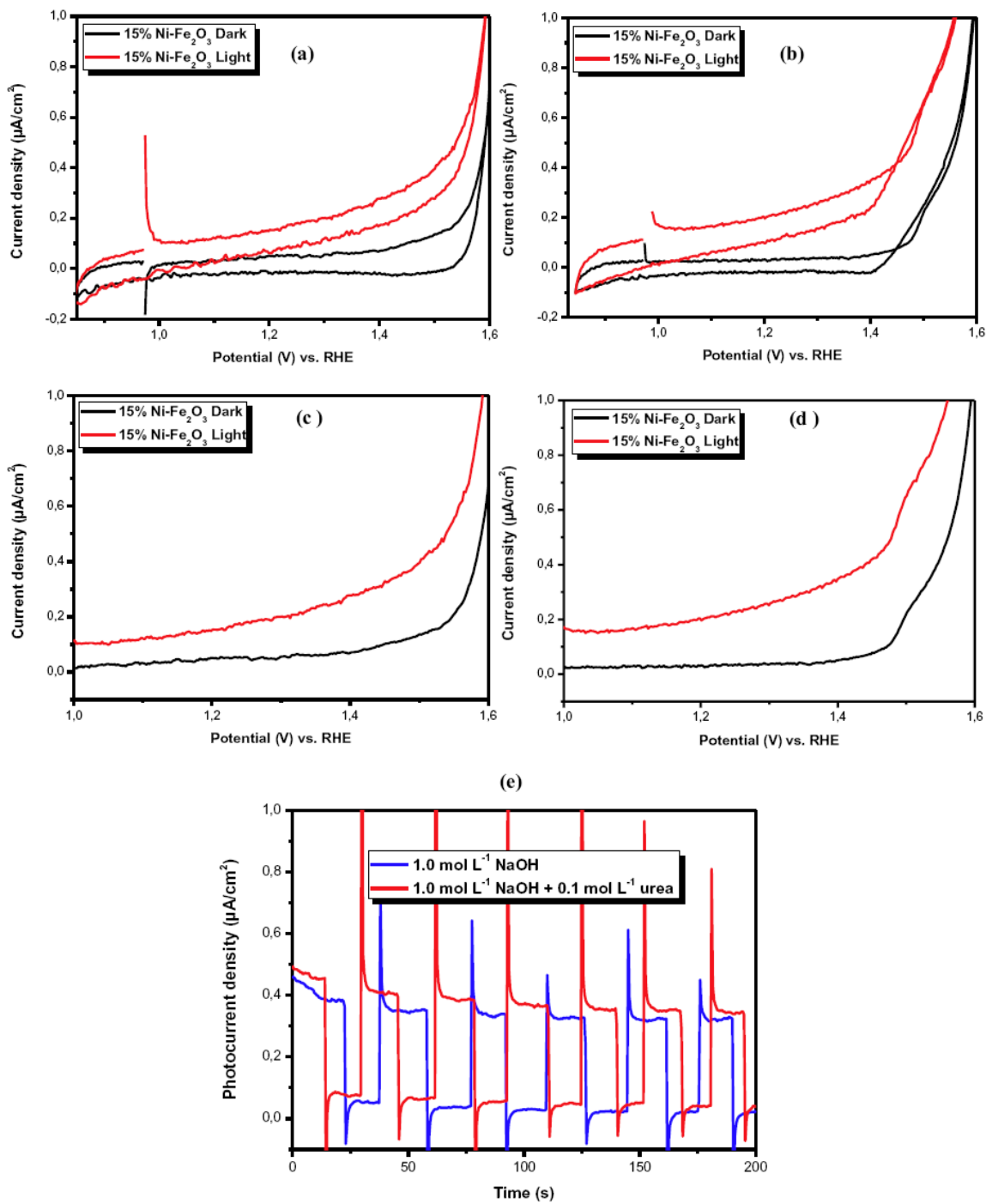


Fig. 7 CV graph **a** in 1.0 M NaOH and **b** in NaOH + 0.1 M urea, LSV graph **c** in 1.0 M NaOH, **d** in NaOH + 0.1 M urea at scan rate of 10 mVs⁻¹ and **e** photocurrent intensity under on/off successive illumination cycles under a bias potential of 1.4 V (vs. RHE) of 15% Ni-Fe₂O₃ photoanode.

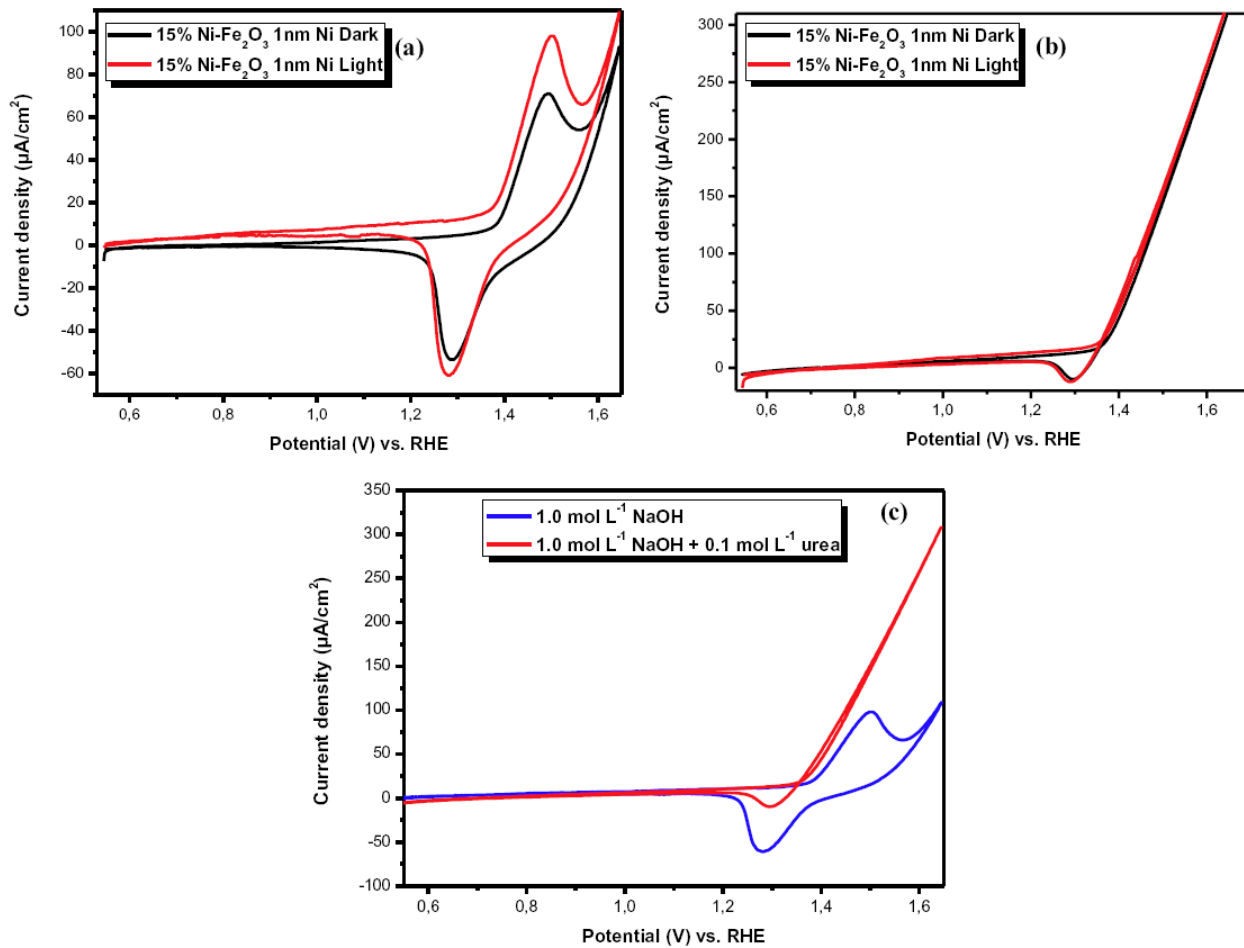


Fig. 8 CV graph in **a** NaOH (1 M), **b** NaOH (1 M) + urea (0.1 M) in dark and with illumination and **c** CV graph in illumination condition of 15% Ni-Fe₂O₃/Ni photoanode at scan rate of 10 mVs⁻¹.

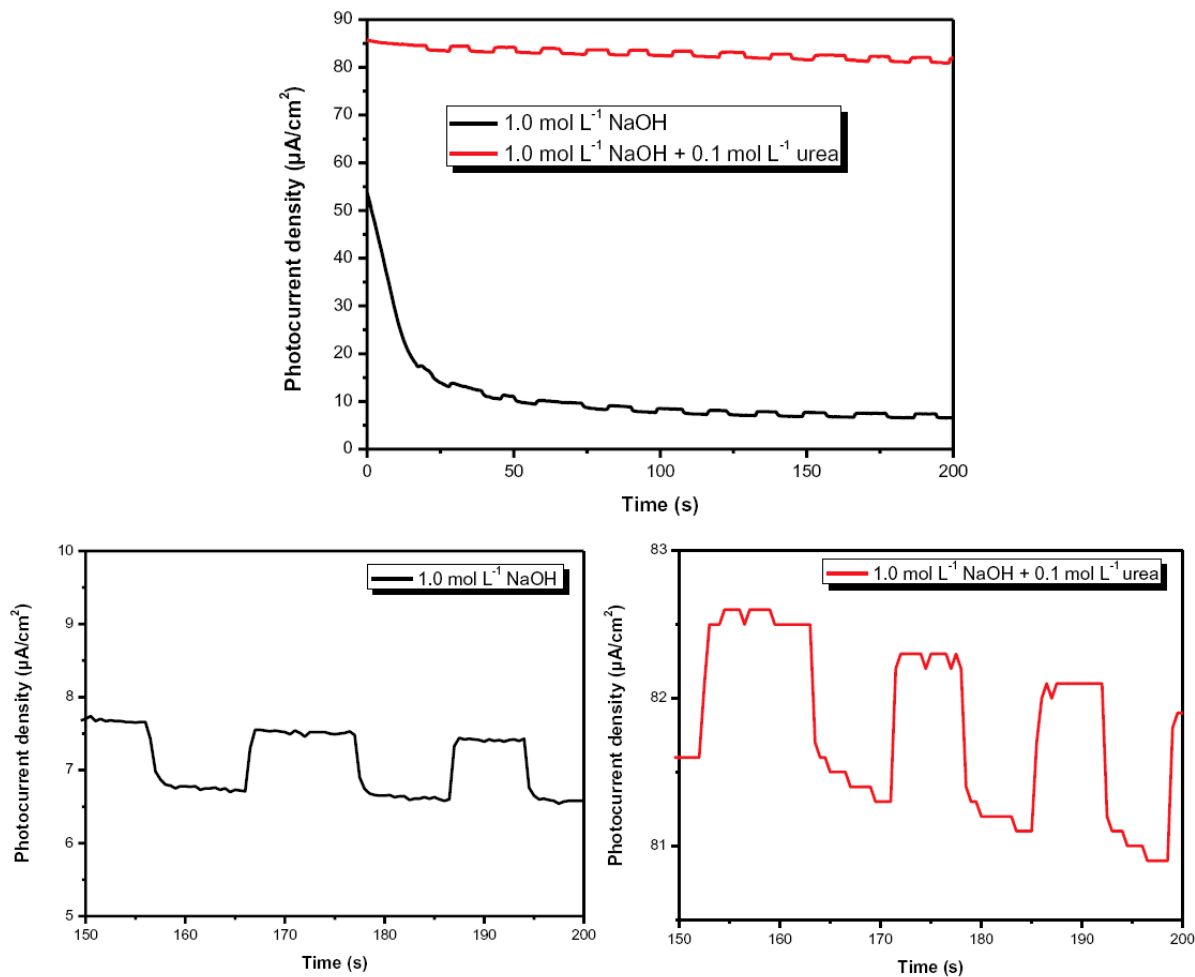


Fig. 9 CA graphs under a bias potential of 1.4 V (vs. RHE) of 15% Ni-Fe₂O₃/Ni.